




## Article

# Carbon Dioxide Decomposition by a Parallel-Plate Plasma Reactor: Experiments and 2-D Modelling

Ali Barkhordari <sup>1,\*</sup>, Saeed Karimian <sup>2</sup>, Antonio Roderó <sup>3,\*</sup>, Dorota Anna Krawczyk <sup>4</sup>, Seyed Iman Mirzaei <sup>5</sup> and Amir Falahat <sup>6</sup>

<sup>1</sup> Faculty of Physics, Shahid Bahonar University of Kerman, Kerman 7616913439, Iran

<sup>2</sup> Department of Physics, Vali-e-Asr University of Rafsanjan, Rafsanjan 7718897111, Iran; Saeed.karimian1373@gmail.com

<sup>3</sup> Department of Physics, University of Cordoba, E-14071 Cordoba, Spain

<sup>4</sup> Department of HVAC Engineering, Bialystok University of Technology, 15-351 Bialystok, Poland; d.krawczyk@pb.edu.pl

<sup>5</sup> Department of Plasma Engineering, Graduate University of Advanced Technology, Kerman 7616913439, Iran; I.mirzaei69@gmail.com

<sup>6</sup> Department of Pilotage, Mahanair UAST University of Kerman, Kerman 7616913439, Iran; Falahatamir@yahoo.com

\* Correspondence: Alibarkhordari20@yahoo.com (A.B.); fa1rosea@uco.es (A.R.)

**Featured Application:** This research is part of a project which aims to investigate the applicability of plasma technologies to air quality. This paper describes the development of a new plasma reactor for CO<sub>2</sub> decomposition that works at atmospheric pressure with AC power. Results for pure CO<sub>2</sub> are presented that elucidate the main mechanisms causing splitting of this molecule in the developed reactor.



**Citation:** Barkhordari, A.; Karimian, S.; Roderó, A.; Krawczyk, D.A.; Mirzaei, S.I.; Falahat, A. Carbon Dioxide Decomposition by a Parallel-Plate Plasma Reactor: Experiments and 2-D Modelling. *Appl. Sci.* **2021**, *11*, 10047. <https://doi.org/10.3390/app112110047>

Academic Editor: Mariusz Jasiński

Received: 2 October 2021

Accepted: 23 October 2021

Published: 27 October 2021

**Publisher's Note:** MDPI stays neutral with regard to jurisdictional claims in published maps and institutional affiliations.



**Copyright:** © 2021 by the authors. Licensee MDPI, Basel, Switzerland. This article is an open access article distributed under the terms and conditions of the Creative Commons Attribution (CC BY) license (<https://creativecommons.org/licenses/by/4.0/>).

**Abstract:** The applicability of high voltage electrical discharges for the decomposition of CO<sub>2</sub> has been extensively demonstrated. In this study, a new AC parallel-plate plasma reactor is presented which was designed for this purpose. Detailed experimental characterization and simulation of this reactor were performed. Gas chromatography of the exhaust gases enabled calculation of the CO<sub>2</sub> conversion and energy efficiency. A conversion factor approximating 25% was obtained which is higher in comparison to existing plasma sources. Optical emission spectroscopy enabled the determination of the emission intensities of atoms and molecules inside the plasma and characterization of the discharge. The Stark broadening of the Balmer hydrogen line H<sub>β</sub> was used for the estimation of the electron density. The obtained densities were of the order of  $5 \times 10^{14} \text{ cm}^{-3}$  which indicates that the electron kinetic energy dominated the discharge. The rotational, vibrational, and excitation temperatures were determined from the vibro-rotational band of the OH radical. A 2-temperature plasma was found where the estimated electron temperatures (~18,000 K) were higher than the gas temperatures (~2000 K). Finally, a 2-D model using the fluid equations was developed for determining the main processes in the CO<sub>2</sub> splitting. The solution to this model, using the finite element method, gave the temporal and spatial behaviors of the formed species densities, the electric potential, and the temperatures of electrons.

**Keywords:** CO<sub>2</sub> conversion; gas chromatography; optical emission spectroscopy; 2-D fluid model

## 1. Introduction

The mitigation of greenhouse gases is one of the most important challenges in the world today. In consequence, finding solutions for carbon dioxide (CO<sub>2</sub>) reduction is a priority research topic. Technologies for the decomposition of these gases after their generation are being developed, together with solutions to reduce CO<sub>2</sub> production at source.

The applicability of high voltage electrical discharge plasmas to reform carbon dioxide (CO<sub>2</sub>) as an environmental pollutant has been extensively studied [1–5]. Plasma discharge

reactors have shown improved efficiency and fewer side effects compared with other existing methods, such as steam methane reforming, steam methane/oxygen reforming, partial oxidation, catalytic partial oxidation, auto-thermal reforming, etc., [5].

Carbon dioxide is a stable and inert molecule that needs a large amount of energy for its splitting which means low energy conversion efficiency. Plasma (ionized gas) is an active medium containing different species including neutral species, ions, electrons, excited species, etc. The ionized species are accelerated by an applied electromagnetic field. Electrons with small mass can reach high energy and produce CO<sub>2</sub> conversion by different impact processes including ionization and vibrational or electronic excitation. New species appear that can favor this conversion. In this way, the energy efficiency is substantially improved [6]. The efficiency of this conversion can be improved with the synergy of a co-reactant that has a higher (less negative) Gibbs free energy; CH<sub>4</sub> ( $\Delta G^\circ = -50.7 \text{ kJ mol}^{-1}$ ) and H<sub>2</sub> ( $\Delta G^\circ = 0 \text{ kJ mol}^{-1}$ ) are the candidates most commonly selected for this purpose [7].

Li et al. [8] studied the variation of CO<sub>2</sub> and CH<sub>4</sub> conversion with the CH<sub>4</sub>/CO<sub>2</sub> ratio using an atmospheric pressure DC corona discharge. A CO<sub>2</sub> conversion of 70% was found for a 2:1 ratio.

A conversion factor approximating 90% was obtained by Li et al. [9] using an atmospheric pressure glow discharge plasma (APGD). In this case, the CH<sub>4</sub>/CO<sub>2</sub> ratio was 4:6. The proposed reactor presented the advantage of large scale treatment and high conversion ability.

In addition, a toroidal transformer-coupled plasma (TCTP) source was used for CO<sub>2</sub> and CH<sub>4</sub> conversion by Li et al. [10]. Optical and mass spectrometric measurements of this source was performed.

Yu et al. [11] evaluated a dielectric packed-bed plasma reactor for CO<sub>2</sub> conversion. The authors showed that the dielectric properties and morphology of packing dielectric pellets notably influenced the electron energy distribution in the formed plasma discharge and the reactions inside the plasma reactor. The effects of the reverse reactions in the CO<sub>2</sub> decomposition and the oxidation of CO were examined. Wang et al. [12] developed a plasma reactor for CO<sub>2</sub> reforming based on dielectric barrier discharge (DBD) with CH<sub>4</sub> and a catalyst. The influences of the different species formed inside the reactor on CO<sub>2</sub> reforming were studied. It was found that the catalyst could substantially improve reduction in CO<sub>2</sub> concentration. The conversion of CO<sub>2</sub> into more valuable chemical products using catalytic plasmas was studied experimentally by Liu et al. [13]. Their results showed that the CO<sub>2</sub> plasma discharges could generate oxygen and other active plasma species for further reaction. In some cases, these reactions lead to the formation of more valuable chemicals such as ethylene, propylene and oxygenates. The experiments also confirmed that the CO<sub>2</sub> plasma was an excellent "catalyst" for the conversion of low alkanes to alkenes. This method was found to be an effective method for the utilization of CO<sub>2</sub> and low alkanes.

This study aims to contribute to the development of new plasma technologies for CO<sub>2</sub> conversion. An AC parallel-plate plasma reactor (AC-PPP) for CO<sub>2</sub> remediation is presented that works at atmospheric pressure and uses alternating current (AC). This reactor has a very simple and low-cost design that can operate at atmospheric pressure, allowing straightforward scaling up for industrial applications. The new design is based on a high voltage (HV) discharge between two parallel electrodes where inlet and outlet metal pipes have been added. This makes it possible to extend the electromagnetic field inside these pipes and expand the treatment area, consequently increasing the conversion efficiency.

A complete experimental and theoretical study of this new reactor was performed to determine its CO<sub>2</sub> remediation ability. The CO<sub>2</sub> conversion factor, CO and O<sub>2</sub> selectivity, and energy efficiency were determined by analyzing the exhaust gases using gas chromatography (GC).

Optical emission spectroscopy confirmed the CO<sub>2</sub> decomposition in this reactor. The former species formed inside the discharge were detected. This technique also made it

possible to determine the characteristic parameters of the plasma including electron density and rotational, vibrational, and excitation temperatures. In consequence, it was possible to determine if the plasma conditions were adequate for the application.

As indicated, the performance of this device was influenced by the spatial distribution of discharge inside the metallic inlet and outlet pipes. A 2-D fluid model was developed to simulate the spatial and temporal behavior of the plasma in all positions of the new AC-PPP reactor. This model allowed determination of the main kinetic mechanisms of CO<sub>2</sub> decomposition in this reactor. The spatial distributions and temporal variations of the different species formed from the CO<sub>2</sub> decomposition were calculated.

## 2. Materials and Methods

### 2.1. Experimental Set-Up

A scheme of the experimental arrangements with the AC-PPP reactor used in this study is shown in Figure 1.

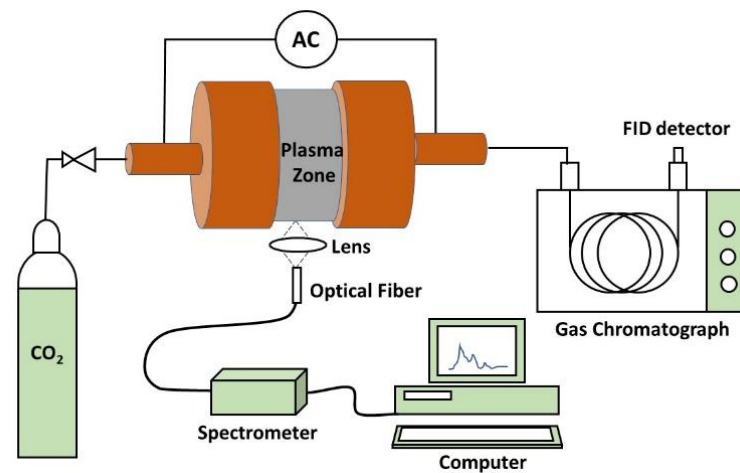


**Figure 1.** Experimental arrangement.

For the manufacture of this reactor, two copper pipes (of 10 mm diameter) were placed axially on both sides of the reactor structure and were connected to the two ring disks (of 50 mm diameter). The pipes performed the role of both gas inlet/outlets and electrodes which were connected to the AC power supply (0–22 kV). The two dielectric cylinders (of 50 mm diameter) were applied to fix these copper pipes. These dielectric cylinders were joined by a Pyrex tube. The axial distance between electrodes was kept at 10 mm (see Figure 2).

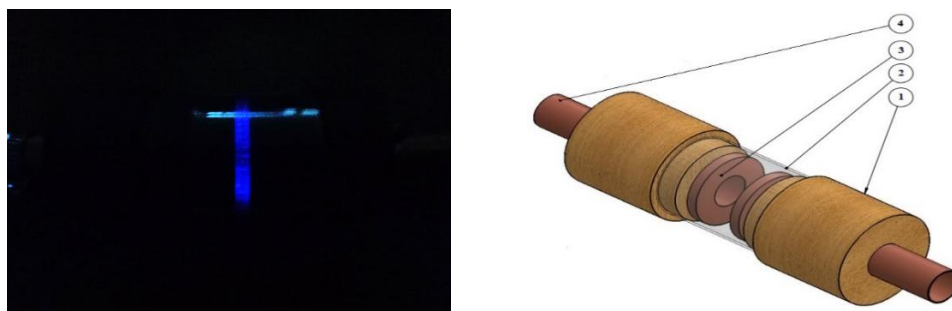


**Figure 2.** Photographic image and the 3D scheme of the AC-PPP reactor: (1) high voltage dielectric, (2) Pyrex tube, (3) copper disk, (4) copper pipe.

A strong electric field was created between the copper electrodes when applying the AC high voltage. The applied voltage varied between 10–22 kV. In this way, a plasma was generated between the electrodes at atmospheric pressure.

The gas entered via one pipe and exited by a separate one. The flow rate of CO<sub>2</sub> gas (purity > 99.5%) was low and constant (~0.15 SLM) to obtain improved control of the applied field. Therefore, the derived axial velocity could be neglected compared to other velocities, i.e., drift and diffusion velocities ( $V_{diff} > V_{drif} \gg V_{axi}$ ).

The application of an electric potential between the two electrodes led to the formation of an axial electric field. Subsequent electron acceleration led to the ionization of background carbon dioxide. During the ionization process, free radicals, ions, and neutral atoms were created inside the AC-PPP reactor. The operating situation of the AC-PPP reactor for a flow rate of 0.15 SLM and an applied voltage fixed of 22 kV is shown in the photographic images in Figure 2.

The consumed power in the discharge was measured with a current probe (Tektronix, Beaverton, OR, USA, TCP202) and a high voltage probe (Tektronix, P6015A) which were connected to an oscilloscope (HM1508).

An HR4000 Ocean Optic spectrometer was used to detect the spectra and perform optical emission spectroscopy (OES). This spectrometer is a compact and flexible device with no moving parts and a linear CCD-array of 3648 pixels. It stores a full spectrum every millisecond with a wavelength range of 200–1100 nm. The optical features of this spectrometer include an input and output focal distance 101.6 mm, spatial groove density grating 2400 line/mm, slit width 5 μm, and optical resolution of width ~0.025 nm.

A confocal quartz lens, with a diameter of 50 mm and focal length of 75 mm, was used to focus the emitted light of the plasma onto the optical fiber probe, which was placed on the focal point of the lens. This lens was focused on the highest intensity positions between electrodes (middle of radial positions,  $r = 15$  mm). This configuration allowed the determination of species present in the plasma and enabled measurement of the plasma parameters, such as electron density, and the rotational, vibrational, and excitation temperatures in this zone.

Gas chromatography was used to study the decomposition of CO<sub>2</sub> and the formation of CO and O<sub>2</sub> compounds. The feed and exhaust gases were analyzed using a compact-gas chromatograph (CGC) type GC, Agilent 6890 N, equipped with a flame ionization detector (FID) and the packed GC columns Molecular Sieve 139 (MS-139) and HayeSep type Q and N. The FID can evaluate hydrocarbons such as propane, acetylene, ethylene, ethane, and others. Moreover, a thermal detector connected by columns, was used to analyze the gas components such as CO<sub>2</sub>, CO, O<sub>2</sub>, etc.

## 2.2. Two-Dimensional Fluid Model

### 2.2.1. Model Equations

For modeling purposes, half of the AC-PPP reactor was considered and azimuthal symmetry around the reactor axis was assumed. Thus, the spatial description of the problem was mathematically two-dimensional (with only axial and radial directions). The simulated domain was the discharge gap between the high-voltage (HV) and ground electrodes. This domain was extended into the conductive inlet/outlet pipes that can affect the electric field distribution (see Figure 3). The grid size was 4.5 μm.

The spatial and temporal macroscopic description of the gas discharge inside the reactor was determined by solving the fluid continuity equations for different species coupled with Poisson's equation. These equations were solved using the finite element method (FEM).

The continuity equation for all the formed species inside the AC reactor is expressed as follows [14]:

$$\frac{\partial n_i}{\partial t} + \nabla \cdot \Gamma_i = \sum_m R_{i,m} \quad (1)$$

where  $n_i$  is the number density,  $\Gamma_i$  expresses the flux for the species  $i$ , and  $R_{i,m}$  are the reaction rates between species  $i$  and species  $m$ .

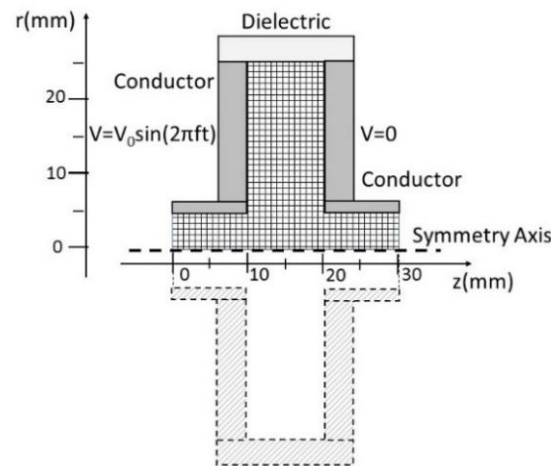


Figure 3. The simulated domain for the AC-PPP reactor in the 2-D model.

For a typical reaction between species



the reaction rate depends on the density of each species,  $n_A$  and  $n_B$ .

$$R = kn_A n_B \tag{3}$$

with  $k$ , the reaction constant [14,15].

In this study, two different approaches were considered to obtain the reaction constants. For some reactions, the experimental data for these reaction rates were available in the literature [16]. In other cases, the reaction rate constants were calculated using the total collision cross sections in terms of the collisional energy,  $\sigma(\epsilon)$ , by the following relationship [17]:

$$k(T) = \frac{1}{k_B T} \left( \frac{8}{\pi \mu k_B T} \right)^{1/2} \int_0^\infty \epsilon \sigma(\epsilon) e^{-\epsilon/k_B T} d\epsilon \tag{4}$$

The collisional cross section can be written as follows:

$$\sigma(\epsilon) = \frac{10^{-13}}{E I_p} \left[ B_1 \ln \left( \frac{\epsilon}{I_p} \right) + \sum_{i=1}^{N-1} B_{i+1} \left( 1 - \frac{I_p}{\epsilon} \right)^i \right] \tag{5}$$

where  $I_p$  is a parameter close (but not always equal) to the ionization or appearance potential for a given ionization channel (expressed in electron-Volts (eV)),  $\epsilon$  is the collision energy (eV),  $B_i$  ( $i = 1, \dots, N$ ) are fitting coefficients, and  $N$  is determined from those conditions for achieving a standard deviation of the fit from data smaller than 3–5% [18].

In the model, only the reactions that showed the greatest influence on the plasma  $\text{CO}_2$  kinetics were considered [19–24]. These reactions were based mainly on the chemistry of Wang [20] and Kozak [23] who provided useful results for gliding arc and microwave plasma, respectively. Table 1 shows the selected reactions inside the AC-PPP reactor. A total of 16 electron collisions and six atomic processes were considered.

The excited  $\text{CO}_2$  states were simplified according to the scheme explained in a previous paper from our group [25]. The levels Va, . . . , and Vd of Table 1 represent the two non-symmetric excited vibrational modes; V1 is the first level of the asymmetric vibrational mode, and the excited electronic states of the  $\text{CO}_2$  are grouped in the effective level  $\text{CO}_2^*$ .

**Table 1.** Selected reactions for different formed species in the AC-PPP reactor.

Num.	Process Name	Reactions	Reaction Rate Constants	Ref.
<i>Electron Collisions</i>				
1	Vibrational Excitation	$e + \text{CO}_2 \rightarrow e + \text{CO}_2(V1)$	$k_1$	[19]
2	Vibrational Excitation	$e + \text{CO}_2 \rightarrow e + \text{CO}_2(Va)$	$k_2$	[19]
3	Vibrational Excitation	$e + \text{CO}_2 \rightarrow e + \text{CO}_2(Vb)$	$k_3$	[19]
4	Vibrational Excitation	$e + \text{CO}_2 \rightarrow e + \text{CO}_2(Vc)$	$k_4$	[19]
5	Vibrational Excitation	$e + \text{CO}_2 \rightarrow e + \text{CO}_2(Vd)$	$k_5$	[19]
6	Electronic Excitation	$e + \text{CO}_2 \rightleftharpoons e + \text{CO}_2^*$	$k_6$	[21]
7	Dissociative De-excitation Collision	$e + \text{CO}_2(Vx) \rightarrow e + \text{CO} + \text{O}$	$k_7$	[19]
8	Electron Ionization	$e + \text{CO}_2 \rightarrow 2e + \text{O}_2 + \text{C}^+$	$k_8$	[19]
9	Electron Dissociation	$e + \text{CO}_2 \rightarrow e + \text{O} + \text{CO}$	$k_9$	[19]
10	Electronic Excitation	$e + \text{CO}_2 \rightleftharpoons e + \text{CO}_2^*$	$k_{10}$	[21]
11	Elastic Collision	$e + \text{CO}_2 \rightleftharpoons e + \text{CO}_2$	$k_{11}$	[21]
12	Electron Ionization	$e + \text{CO}_2 \rightleftharpoons 2e + \text{CO}_2^+$	$k_{12}$	[22]
13	Electron Ionization	$e + \text{CO}_2 \rightarrow 2e + \text{CO} + \text{O}^+$	$k_{13}$	[22]
14	Dissociative Electron-Ion Recombination	$e + \text{CO}_2^+ \rightarrow \text{CO} + \text{O}$	$k_{14}$	[22]
15	Dissociative Attachment	$e + \text{CO}_2 \rightleftharpoons \text{CO} + \text{O}^-$	$k_{15}$	[23]
16	Electron Dissociation	$e + \text{O}_2 \rightarrow e + 2\text{O}$	$k_{16}$	[23]
<i>Atomic Collisions</i>				
17	Neutral Dissociation	$\text{O} + \text{CO}_2 \rightarrow \text{CO} + \text{O}_2$	$k_{17}$	[20]
18	Charge Exchange	$\text{CO}_2 + \text{CO}_2^+ \rightleftharpoons \text{CO}_2^+ + \text{CO}_2$	$k_{18}$	[20]
19	Scattering	$\text{O} + \text{O}_2 \rightarrow \text{O} + \text{O}_2$	$k_{19}$	[20]
20	3-body Recombination	$\text{O} + \text{O} + \text{CO}_2 \rightarrow \text{O}_2 + \text{CO}_2$	$k_{20}$	[23]
21	3-body Neutral-Neutral Collision	$\text{O} + \text{C} + \text{CO}_2 \rightarrow \text{CO} + \text{CO}_2$	$k_{21}$	[24]
22	3-body Neutral-Neutral Collision	$\text{O} + \text{CO} + \text{CO}_2 \rightarrow \text{CO}_2 + \text{CO}_2$	$k_{22}$	[24]

The flux term in the continuity fluid equations for all species (Equation (1)) was based on the momentum conservation of each species. The corresponding flux term for each species  $i$  depends on its electrical mobility,  $\mu_i$ , and spatial diffusivity,  $D_i$ , i.e.,

$$\Gamma_i = \pm \mu_i n_i \mathbf{E} - D_i \nabla n_i \quad (6)$$

The plus or minus sign in this equation corresponds to the sign of the charged particles [1,26].

Only the mobility coefficients for ions and electrons were included [27]. The mobility of ions was calculated according to the Langevin equation:

$$\mu_i = 0.514 m_i^{1/2} \frac{T_g}{P_{tot}} \alpha_i^{-1/2} \quad (7)$$

where  $\alpha_i$  is the polarization of background gas per unit of cubic angstroms; its value for various gases is presented in the existing literature on gaseous discharges [27]. In this work, the mobilities for  $\text{CO}_2^+$  and  $\text{C}^+$  species were 0.0012 and 0.0009  $\text{m}^2/\text{Vs}$ , respectively.

The diffusion coefficient of the electrons and ions were instead calculated from the Einstein relation:

$$D_{e(i)} = \frac{k_B T_{e(i)}}{q_{e(i)}} \mu_{e(i)} \quad (8)$$

with  $T_{e(i)}$  and  $q_{e(i)}$  being the temperature and charge of electrons and ions [28].

For neutral species, the diffusion coefficients were calculated using the distribution coefficients of Lennard–Jones [29].

The rate of change of the electron energy density is described by [1]:

$$\frac{\partial \omega_e}{\partial t} + \nabla \cdot \Gamma_\omega + eE \cdot \Gamma_e = R_\omega \quad (9)$$

where  $\omega_e$  is the electron energy density,  $R_\omega$  is the energy loss or gain due to inelastic collisions, the term  $eE \cdot \Gamma_e$  accounts for the ohmic or joule heating of the electrons in the electric field, and  $\Gamma_\omega$  is the electron flux energy, that is described by:

$$\Gamma_\omega = \frac{5}{3} (-\mu_e \omega_e E - D_e \nabla \omega_e) \quad (10)$$

The electron energy loss or gain  $R_\omega$  is obtained by summing the collisional energy loss or gain over all reactions [14]:

$$R_\omega = \sum_{j=1}^P x_j k_j N_n n_e \Delta \varepsilon_j \quad (11)$$

where  $x_j$  is the mole fraction of the target species for reaction  $j$ ,  $k_j$  is the rate coefficient for reaction  $j$ ,  $N_n$  is the total neutral number density and  $\Delta \varepsilon_j$  is the energy loss from reaction  $j$ .

The electron energy density  $\omega_e$ , the mean electron energy  $\varepsilon$ , and the electron temperature  $T_e$  are correlated with each other through [30]:

$$\omega_e = n_e \varepsilon = \frac{3}{2} k_B n_e T_e \quad (12)$$

For non-electron species, the following equation was solved for the mass fraction of each species [30]:

$$\rho \frac{\partial \zeta_k}{\partial t} + \rho (\mathbf{u} \cdot \nabla) \zeta_k = \nabla \cdot \mathbf{j}_k + R_k \quad (13)$$

where  $\mathbf{j}_k$  is the diffusive flux vector,  $R_k$  is the rate expression for species  $k$ ,  $\mathbf{u}$  is the mass averaged fluid velocity vector,  $\rho$  denotes the density of the mixture and  $\zeta_k$  is the mass fraction of the  $k$ th species.

The diffusive flux vector is defined as [30]:

$$\mathbf{j}_k = \rho \zeta_k \mathbf{V}_k \quad (14)$$

with  $\mathbf{V}_k$ , being the multicomponent diffusion velocity for species  $k$ .

To initiate discharge in the reactor, electric potential should be applied between the electrodes, thus Poisson's equation must also be considered in the model [14]:

$$\varepsilon_0 \nabla^2 \varphi = -\sigma \quad (15)$$

where  $\varphi$  is the electric potential,  $\varepsilon_0$  is the vacuum permittivity and  $\sigma$  is the charge density, that can be written in terms of density of the charged species,  $n_k$ , and their charge,  $eZ_k$  [31]:

$$\sigma = e \left( \sum_{k=1}^k Z_k n_k - n_e \right) \quad (16)$$

In this work, 16 different neutral and ionized species were considered in the model (Table 2). Thus, 16 continuity equations together with Poisson’s equation were solved with the employment of a stabilized FEM.

**Table 2.** Species considered in the model.

Neutrals	CO, CO <sub>2</sub> , O <sub>2</sub> , O, C
Pos. ions	CO <sub>2</sub> <sup>+</sup> , C <sup>+</sup> , O <sup>+</sup> , O <sub>2</sub> <sup>+</sup>
Neg. ions	O <sup>-</sup>
Elec. excited	CO <sub>2</sub> <sup>*</sup>
Vib. excited	CO <sub>2</sub> (V <sub>a...d</sub> ), CO <sub>2</sub> (V <sub>1</sub> )

### 2.2.2. Boundary Conditions

To obtain a unique solution for the system of coupled equations with the geometry presented in Figure 3, the boundary conditions (Dirichlet and Neumann boundary conditions) must be imposed. The boundary conditions applied for the AC plasma reactor corresponded to those found in the existing literature [32]. The following boundary condition was used to account for the particle flux in walls:

$$\Gamma_i \cdot n = \left( a_i \operatorname{sgn}(q_i) \mu_i E \cdot n + \frac{1}{4} v_{th(i)} \right) n_i \tag{17}$$

where  $n$  is the normal vector pointing toward the tube wall and,  $v_{th(i)}$  is the thermal velocity of particles [32]:

$$v_{th(i)} = \sqrt{\frac{8k_B T_i}{\pi m_i}} \tag{18}$$

and the number  $a_i$  is defined by:

$$a_i = \begin{cases} 1 & \operatorname{sgn}(q_i) \mu_i E \cdot n \geq 0 \\ 0 & \operatorname{sgn}(q_i) \mu_i E \cdot n \leq 0 \end{cases} \tag{19}$$

For electrons, as a special case, the particle flux due to secondary electron emission (SEE) was added to the system and is defined as follows [32]:

$$\Gamma_e \cdot n = \left( -a_e \mu_e E \cdot n + \frac{1}{4} v_{th,e} \right) n_e - \sum_p \gamma_p \Gamma_p \cdot n \tag{20}$$

where  $\gamma_p$  are the SEE coefficients, which defines the average number of electrons emitted per impact of ions  $p$  on the tube wall.

Similarly, a boundary condition for electron energy was [32]:

$$\Gamma_\omega \cdot n = -\frac{5}{6} v_{th,e} \omega_e - \sum_p \gamma_p \varepsilon_p (\Gamma_p \cdot n) \tag{21}$$

Here, the second term is the SEE energy flux, being  $\varepsilon_p$  the mean energy of the secondary electrons.

The discharge was driven by a sinusoidal electric potential applied to an electrode and the other electrode was grounded. Then the boundary condition of electric potential in the grounded electrode was:

$$\varphi = 0 \tag{22}$$

and the electric potential in the powered electrode was given by:

$$\varphi = V_0 \sin(2\pi ft) \tag{23}$$



with  $f = 50$  Hz and  $V_0 = 22$  kV.

### 3. Results and Discussion

#### 3.1. Experimental Results

##### 3.1.1. Gas Chromatography

The inlet and outlet gases were analyzed with the gas chromatograph GC, Agilent 6890 N. The areas of chromatogram peaks are proportional to the concentrations of compounds in these gases. Then, the CO<sub>2</sub> conversion factor can be calculated from the areas of CO<sub>2</sub> peak,  $[CO_2]_{in}$  and  $[CO_2]_{out}$  by [33]:

$$X_{CO_2}(\%) = \frac{[CO_2]_{in} - [CO_2]_{out}}{[CO_2]_{in}} \times 100 \quad (24)$$

In a similar way, the selectivity of CO and O<sub>2</sub> species were calculated by [32]:

$$S_{CO}(\%) = 0.5 \frac{[CO]_{out}}{[CO_2]_{in} - [CO_2]_{out}} \times 100 \quad (25)$$

$$S_{O_2}(\%) = \frac{[O_2]_{out}}{[CO_2]_{in} - [CO_2]_{out}} \times 100$$

Figure 4a shows the conversion factor of CO<sub>2</sub> and the selectivity of CO and O<sub>2</sub> obtained by gas chromatography for an applied voltage between 10 and 22 kV. A maximum value of the conversion factor of 25% was found at 22 kV voltage. This factor was also compared with that obtained by the 2-D model (see Section 3.2).

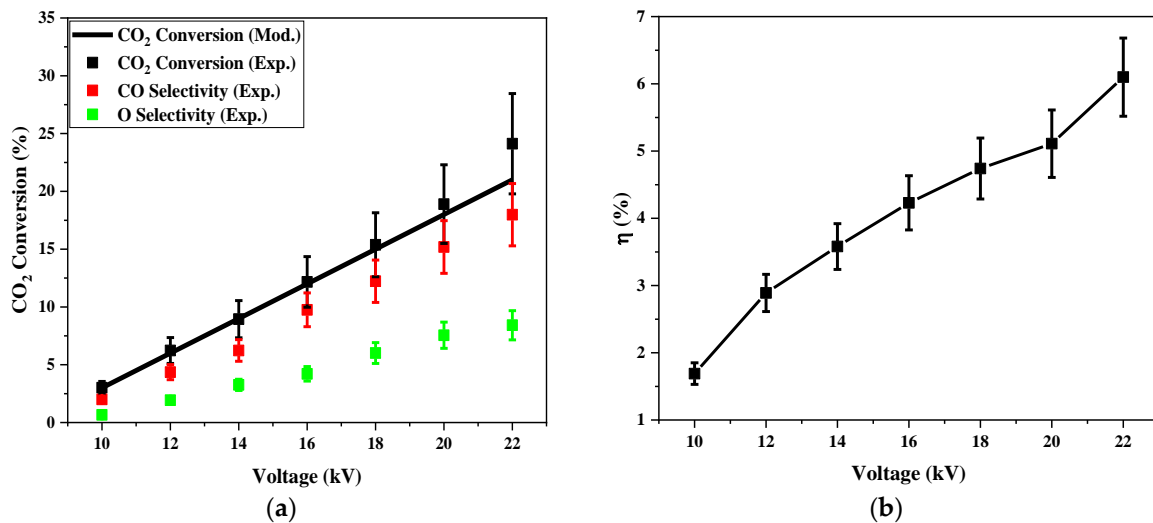


**Figure 4.** (a) Dependence of CO<sub>2</sub> conversion and CO/O<sub>2</sub> selectivity on applied AC voltage. (b) Experimental dependence of energy efficiency on applied AC voltage.

The energy efficiency of this technique is given by [32]:

$$\eta(\%) = X_{CO_2}(\%) \frac{\Delta H_R}{SEI * V_m} \quad (26)$$

where  $V_m$  is the molar volume, that can be considered 24.5 L/mol,  $\Delta H_R$  is the reaction enthalpy for CO<sub>2</sub> splitting ( $CO_2 \rightarrow CO + \frac{1}{2}O_2$ ), i.e., 279.8 kJ/mol, and SEI is the specific energy input, that is calculated from discharge power and gas flow rate:

$$SEI = \frac{Power}{Flow} \quad (27)$$

The power consumed in discharge was estimated from measurements of the electrical current and HV voltage between the electrodes of the AC-PPP reactor. Then the energy

efficiency could be calculated. Table 3 shows the values of this efficiency for different applied voltages. In this case, the maximum efficiency was 6.1% for an applied voltage of 22 kV. This experimental energy efficiency of CO<sub>2</sub> conversion is plotted in Figure 4b.

**Table 3.** The average consumed power and energy efficiency for different applied voltages.

Applied Voltage (kV)	Power (W)	$\eta$ (%)
10	50.95	1.69
12	61.60	2.89
14	71.35	3.58
16	82.14	4.23
18	92.64	4.74
20	105.49	5.11
22	113.05	6.1

In the review paper by Snoeckx et al. [7], a comparison of the conversion factor and the energy efficiency of different plasmas technologies for CO<sub>2</sub> remediation was performed. Typical plasma technologies used for this purpose are dielectric barrier discharges (DBDs), microwave discharges (MWs), and gliding arc discharges (GAs). These systems are compared with the proposed AC-PPP reactor in Table 4.

**Table 4.** Comparison of CO<sub>2</sub> conversion factor and energy efficiency for different plasma technologies [7].

Technology	Range of CO <sub>2</sub> Conversion (%)	Range of Energy Efficiency (%)
Dielectric Barrier Discharges	0–30	0–15
Microwave Discharges	0–80	0–40
Gliding Arc Discharges	0–10	0–30
AC-PPP Reactor *	2.5–25	1–6

\* Results of this work.

In general, the DBD plasma has a high conversion factor, but it is not energy efficient. Its maximum energy efficiency values were approximately 6%. The MW is the technology with the highest CO<sub>2</sub> conversion with systems that have up to 80% energy efficiency. Some systems can also achieve a high energy efficiency of 40%, but the typical values for this technology are less than 10%. The power consumption of this system is usually very high. The worst CO<sub>2</sub> conversion is obtained for the GA discharge. The reactor introduced in this study had a conversion factor value greater than GA and close to the maximum for DBD. Energy efficiency is low compared to the other technologies, but it has the advantages of its simple design and low power consumption, which are important factors for its industrial implementation.

### 3.1.2. Optical Emission Spectroscopy

In the plasma discharge media, the collision process excites several plasma species to upper states decaying and emitting photons with various specific wavelengths. By recording the emission spectra of the plasma discharge medium, these photons can be detected and analyzed.

In this work, the OES technique was used to identify the different reactive species produced between the electrodes of the CO<sub>2</sub> plasma reactor. Vibro-rotational bands of CO<sub>2</sub>, CO<sub>2</sub><sup>+</sup>, C<sub>2</sub>, and CO radicals and atomic lines of oxygen were detected (see Figure 5 and Table 5). Vibro-rotational bands of radical ·OH and the H<sub>β</sub> emission line of hydrogen, coming from small water impurities in the inlet gas, were also identified. The amount of this water was so small that it had no relevant influence on the plasma.

**Table 5.** Detected peaks for the AC-PPP reactor with CO<sub>2</sub> gas.

Species	$\lambda$ (nm)	Transition Name	Transition Symbol	$v'$	$v''$
OH(Q)	306–312	Molecular Transition	$A^2\Sigma \rightarrow X^2\Pi$	0	0
	326.1	Fox, Duffendack and Barker's System	$X^2\Pi_g \rightarrow A^2\Pi_u$	3	1a
CO <sub>2</sub>	338.3	Fox, Duffendack and Barker's System	$X^2\Pi_g \rightarrow A^2\Pi_u$	2	0
	368.2	Fox, Duffendack and Barker's System	$X^2\Pi_g \rightarrow A^2\Pi_u$	1	2
CO <sub>2</sub> <sup>+</sup>	387.5	Fox, Duffendack and Barker's System	$X^2\Pi_g \rightarrow A^2\Pi_u$	2	4
	407.3	Fox, Duffendack and Barker's System	$X^2\Pi_g \rightarrow A^2\Pi_u$	1	4
H	486.1	H $_{\beta}$ Balmer series line	$n = 4 \rightarrow n = 2$	-	-
	656.3	H $_{\alpha}$ Balmer series line	$n = 3 \rightarrow n = 2$	-	-
C <sub>2</sub>	471.6	Swan System	$A^3\Pi_g \rightarrow B^3\Pi_u$	0	1
	516.4	Swan System	$A^3\Pi_g \rightarrow B^3\Pi_u$	0	0
	560.1	Swan System	$A^3\Pi_g \rightarrow B^3\Pi_u$	1	0
CO	589.5	High Pressure Bands	$A^3\Pi_g \rightarrow B^3\Pi_u$	6	8
	458.5	The Triplet Bands	$d^3\Pi \rightarrow a^3\Pi$	6	0
	564.2	The Triplet Bands	$d^3\Pi \rightarrow a^3\Pi$	2	0
	601.4	The Triplet Bands	$d^3\Pi \rightarrow a^3\Pi$	1	0
CO <sup>+</sup>	643.2	The Triplet Bands	$d^3\Pi \rightarrow a^3\Pi$	0	0
	427.3	Comet-tail system (First Negative System)	$X^2\Pi \rightarrow A^2\Sigma$	2	0
O <sub>2</sub>	385.3	Chamberlains Airglow System	$a^1\Delta_g \rightarrow C^3\Delta_u$	0	1
O <sub>2</sub> <sup>+</sup>	550–600	Molecular emission Band	$B^4\Sigma_g^- \rightarrow A^4\Pi_u$	0	1
O	777.1	Atomic Transition	$3p^5P \rightarrow 3s^5S$	-	-
	843.2	Atomic Transition	$3p^3P \rightarrow 3s^3S$	-	-

A study of the dependencies of the normalized intensities of the headband of vibro-rotational bands of these formed species and the oxygen atomic line 771.1 nm on the plasma position was carried out. Figure 6 plots these dependencies for an applied voltage of 22 kV and a frequency of 50 Hz. The intensity of CO<sub>2</sub> species was higher than that of other species although it was reduced close to the electrodes. Furthermore, the intensities of CO, O, OH, and C<sub>2</sub> species increased near the electrodes but they had a minimum value at the middle of discharge. The relative intensities of Figure 6 are not directly related to the populations of these species because these are affected by many parameters, such as electron density, the cross sections of particles, etc.; however, it is indicative of the presence of species between the reactor electrodes.

The density and temperature of particles in the plasma are the most fundamental parameters in the physical characteristics of gas discharges and play a very important role in understanding the discharge physics and optimization of the operating parameters of the plasma reactor. From an experimental point of view, these parameters are commonly measured using different techniques including Langmuir probes, microwave interferometry, laser Thomson scattering, and optical emission spectroscopy (OES) techniques [34].

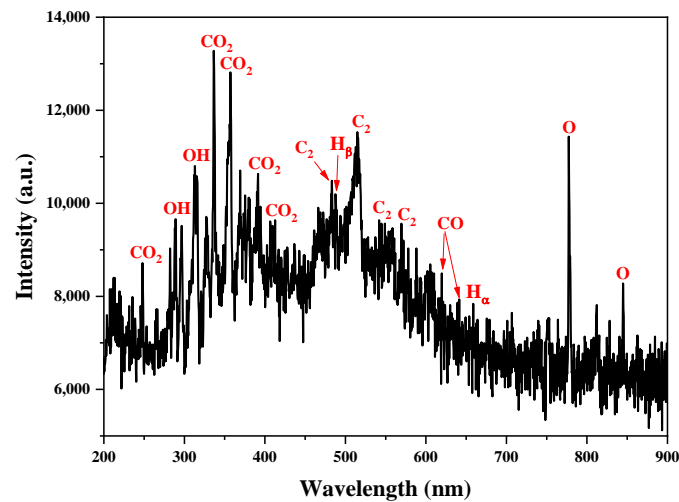


Figure 5. Emission spectrum of the AC-PPP at the AC voltage of 22 kV and the position  $z = 5$  mm.

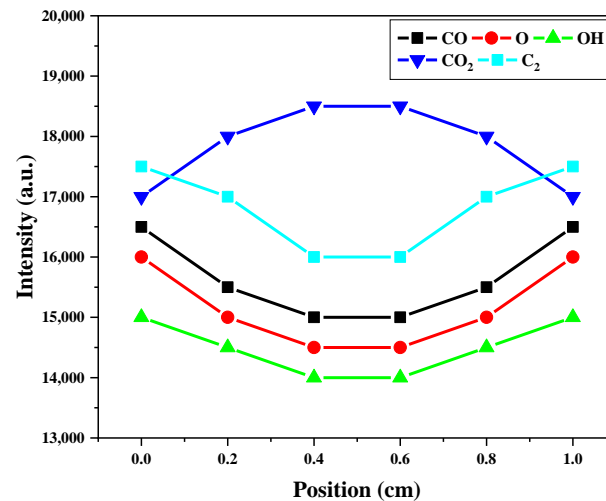


Figure 6. Relative intensities for emission lines of various species as a function of position at an AC voltage of 22 kV and 1 cm distance between electrodes.

#### Rotational, Vibrational, and Excitation Temperatures

As indicated, the OH emission band ( $A^2\Sigma \rightarrow X^2\Pi$ ) was detected in the wavelength ranges of 306–312 nm. The formation of the ·OH radical is generally caused by water vapor molecules that are present as impurities in the gas [35,36]. The rotational, vibrational, and electronic states of this radical are populated by inelastic collisions with particles within the plasma (heavy particles and electrons) which produce variations in their energies.

The rotational temperature gives the population distribution of rotational states. For these states, which have a small separation in energy, the effect of collisions with heavy particles are predominant; the population of rotational states is given by the energy of these particles. In equilibrium conditions, the rotational temperature is considered a good approximation of the gas temperature (mean kinetic temperature of heavy particles).

On the other hand, the population of vibrational and electronic states, with higher energy separation, is given mainly by collisions with electrons. In this case, the obtained vibrational and excitation temperatures can be considered a closer approximation to the electron temperature.

In this work, the emission spectrum of the OH  $A^2\Sigma \rightarrow X^2\Pi$  band was used for the determination of the rotational, vibrational, and excitation temperatures in the AC plasma reactor. Figure 7a shows an example of this spectrum in the AC plasma reactor at the applied AC voltage of 22 kV. Rotational, vibrational, and excitation temperatures were

calculated using SPECAIR software that fits a simulated spectrum to experimental data to estimate these temperatures (see Figure 7a) [26]. For this simulation work, all the factors affecting the line shape, such as the instrumental resolution or the collisional broadenings, were considered.

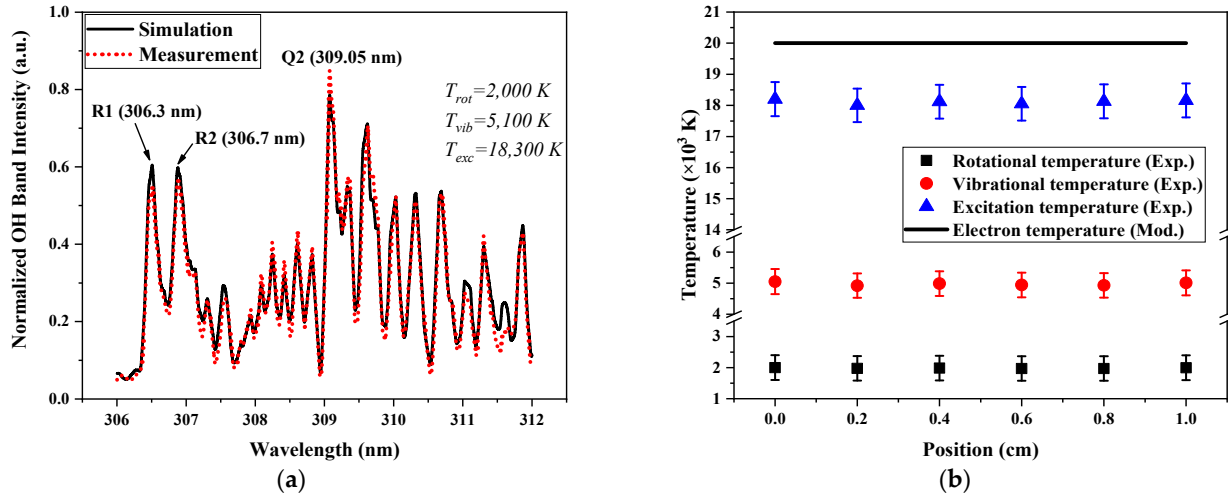


**Figure 7.** (a) Experimental emission spectrum of the OH  $A^2\Sigma \rightarrow X^2\Pi$  band (dots) with their SPECAIR fitting (line) for the determination of the rotational, vibrational, and excitation temperatures. (b) Variations of rotational, vibrational, and excitation temperatures as a function of position at the AC voltage of 22 kV and 1 cm distance between electrodes.

By applying this fitting to vibro-rotational bands, the rotational, vibrational, and excitation temperatures were obtained in terms of position with an error of 7% (Figure 7b). For the three temperatures, their values were constant along the reactor, due to the parameters oscillating between the electrodes during the cycle of AC voltage (see next section). These results correspond to time average values during this cycle.

Figure 7b shows that the experimental rotational temperature was about 2000 K for all positions. The vibrational and excitation temperatures were about 5000 K and 18,000 K, respectively, which means the plasma was in 2-T conditions, where the electron temperature was higher than the gas temperature. The energy of the heavy particles and electrons were enough to produce the conversion of the  $\text{CO}_2$  molecules.

#### Electron Number Density

To find out whether the electron collisions are the main cause of molecule dissociation in the formed discharges, the electron number density was experimentally calculated in the plasma positions focused on by the lens.

The Stark broadening analysis of the spectral profile of the  $H_\beta$  emission line (486.1 nm) is the most usual procedure for the experimental determination of electron density in a plasma discharge [37]. The Stark broadening of this line depends on electron density according to the expression [38]:

$$\Delta\lambda_{stark} = 2 \times 10^{-11} \left( n_e^{2/3} \right) \quad (28)$$

where density is in  $\text{cm}^{-3}$  and Stark broadening is in nm.

The pressure broadening occurs when the energy states of the emitting species are disturbed by the neutral species in the plasma discharge. This broadening depends on resonance and van der Waals effects. In this experiment, the hydrogen atom density was very

low, and the resonance effect can be neglected. Thus, the van der Waals broadening was the only contribution to the pressure broadening, which can be described as follows [39–41]:

$$\Delta\lambda_{Pressure} = \Delta\lambda_{van\ der\ Waals} = 8.18 \times 10^{-26} \lambda^2 \left( \alpha \langle R^2 \rangle \right)^{2/5} \left( \frac{T_g}{\mu} \right)^{3/10} \frac{P}{kT_g} \quad (29)$$

where  $\mu$  is the reduced mass of the colliding particles ( $\mu = 0.92308$  for H/CO<sub>2</sub> collision),  $\lambda$  is the wavelength of the  $H_\beta$  line (486.1 nm),  $\alpha$  is the molecular polarizability of the CO<sub>2</sub> disturbing particles ( $\alpha = 2.46 \times 10^{-24}$  cm<sup>3</sup>),  $\langle R^2 \rangle$  is the difference of the squared radius of the upper and lower levels of  $H_\beta$  transition,  $T_g$  is the gas temperature in K, and  $P$  is the pressure (1 atm for atmospheric pressure).

The Stark and pressure broadenings are the main contributions to the Lorentz shape of a line. So, the full-width at half-maximum (FWHM) value of the Lorentz profile can be obtained from these broadenings [42]:

$$\Delta\lambda_{Lorentz} = \Delta\lambda_{Stark} + \Delta\lambda_{Pressure} \quad (30)$$

Another contribution to the line broadening is the Doppler effect through particle movement. This broadening has a Gaussian profile and can be written as follows [42]:

$$\Delta\lambda_D(nm) = 7.2 \times 10^{-7} \sqrt{\frac{T_g}{M}} \lambda \quad (31)$$

where  $\lambda$  is the wavelength of  $\beta$  hydrogen line (486.1 nm),  $M$  is the molar weight of hydrogen, which is equal to 1, and  $T_g$  is the gas temperature in Kelvin units.

The total Gaussian profile is generally considered as a convolution of Doppler and instrumental profiles, then [43]:

$$\Delta\lambda_G = \sqrt{\Delta\lambda_D^2 + \Delta\lambda_I^2} \quad (32)$$

where  $\Delta\lambda_G$  and  $\Delta\lambda_I$  are the Gaussian and instrumental broadenings, respectively. The optical components resolution directly affects the instrumental broadening.

A convolution of these Gaussian and Lorentzian profiles results in a Voigt shape. Fitting of experimental data to this analytical curve allowed us to separate Lorentz and Gaussian contributions (Figure 8a). In this study, Origin software was used for this purpose. In this way, the FWHM of the Lorentzian broadening could be distinguished.

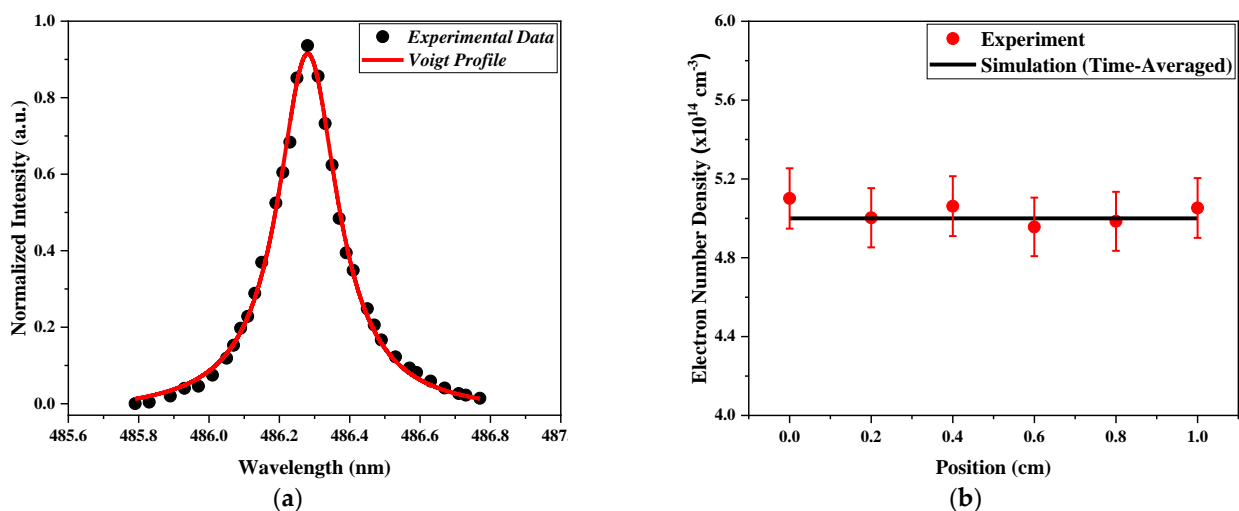


**Figure 8.** (a) Detected  $H_\beta$  emission line with its fitting to a Voigt profile. (b) Variations of electron density as a function of position at the AC voltage of 22 kV and 1 cm distance between electrodes.

The Stark broadening and, consequently, the plasma electron density could be calculated via Equations (28) and (30), respectively.

Figure 8b shows the experimental values of the electron density obtained in this way. A constant distribution along the discharge was again obtained. The experimental value of electron density was of the order of  $5 \times 10^{14} \text{ cm}^{-3}$ . This high value supports the electron kinetics for  $\text{CO}_2$  decomposition assumed for this reactor.

### 3.2. Model Results

The considered continuity model for such a plasma reactor contributes to understanding the chemical and dynamical behaviors of the charged particles inside the reactor. Using the FEM, the equation system described in Section 2.2.1 was solved. This system corresponds to the continuity equation for each species considered in the model (Equation (1)), the energy equation for electrons (Equation (9)), and Poisson's equation for the electric field (Equation (15)). For studying the non-electron species (neutral species), the mass fraction equation should be solved (Equation (13)). Therefore, the temporal and spatial behaviors of these species inside the  $\text{CO}_2$  plasma reactor were calculated. The simulation parameters used in these calculations are presented in Table 6.

**Table 6.** The simulation parameters.

Symbol	Value
Mobility, $\mu_e$ , $\text{m}^2/\text{Vs}$ (for electrons)	1.28
Initial temperatures, $T$ , eV (for electron and heavy particles)	0.54, 0.026
Potential amplitude, KV	22
Diffusion coefficient (for electrons)	0.033
Initial density, $\text{cm}^{-3}$ (charged species)	$10^{10}$
Initial density, $\text{cm}^{-3}$ (background species)	$10^{19}$
Total time, ms	20
Time steps, ns	1

To show the time evolution of the discharge, the results of the plasma simulation for five different times during the AC cycle are presented in the following subsections. Figure 9 plots the selected time against the applied HV voltage.

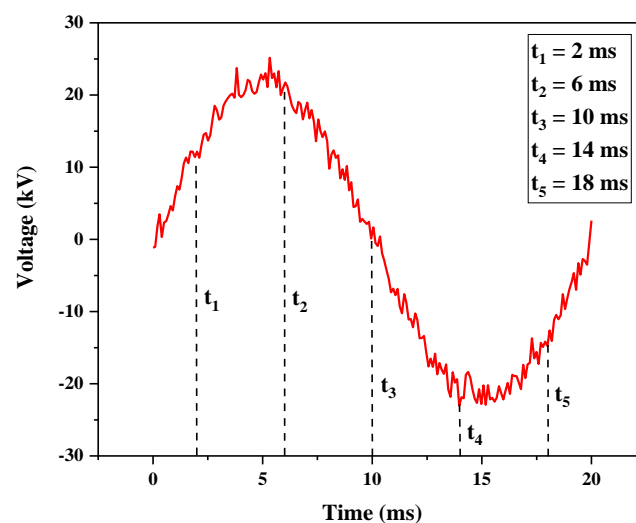


**Figure 9.** Applied HV voltage with the selected times for the presentation of the model results.

### 3.2.1. Electric Potential

Figure 10 shows variations of the electric potential as a function of position at times 2, 6, 10, 14, and 18 ms. The electric potential presents the highest gradient near the electrodes, which is due to electron accumulation at the anode shielding the electric field. This sheath formation has also been found in other contact-electrode plasmas, such as DBD [44–46]. Higher electric potential gradients at the electrodes gave a higher electric field in these positions. The electric field was able to reach a value of 4000 kV/m for 22 kV near the electrodes, decreasing to 1000 kV/m in the zone between them. Inside the inlet and outlet metal pipes, the potential was almost constant, which means the electric field was zero in these zones.

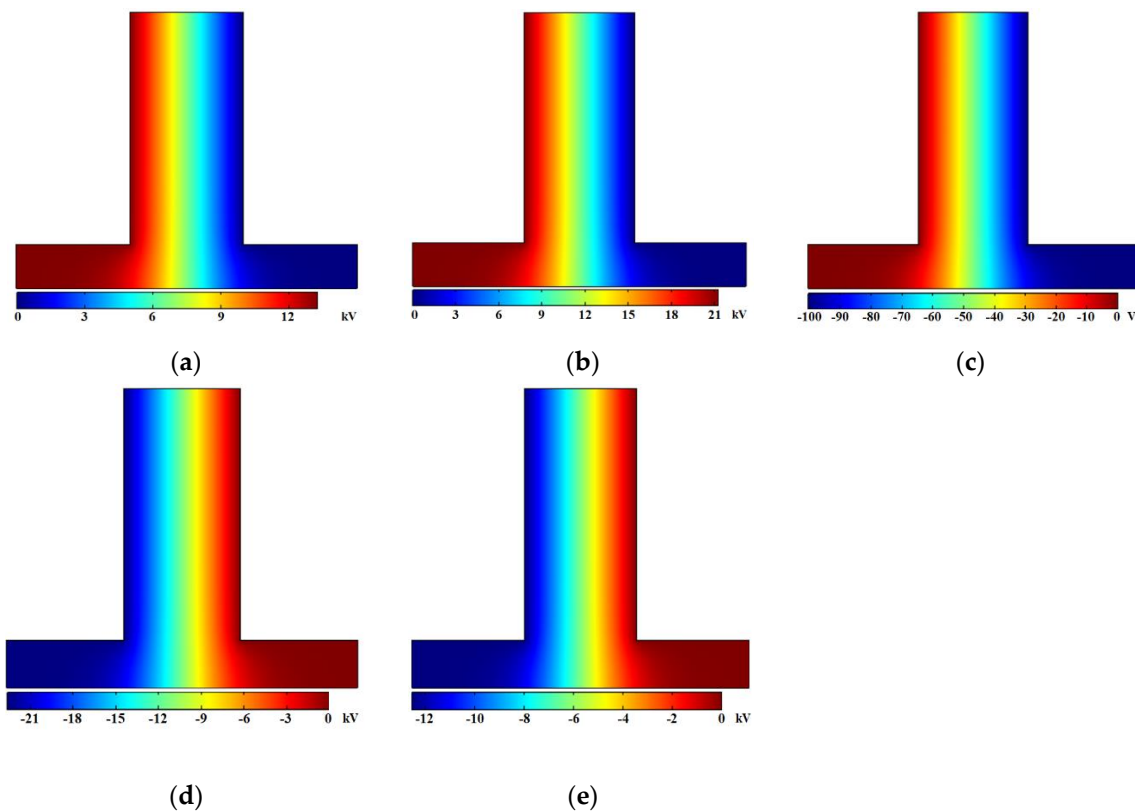


**Figure 10.** Spatial distribution of the electric potential for times (a) 2 ms, (b) 6 ms, (c) 10 ms, (d) 14 ms and (e) 18 ms for the reactor at 22 kV AC voltage and 1 cm distance between electrodes.

When the applied HV voltage was changed, the potential oscillated between electrodes according to the voltage variation, maintaining similar spatial distribution behavior (see different times in Figure 10).

### 3.2.2. Electron Density

After applying the electric field, ionization of species was started inside the AC-PPP reactor, producing electrons, which are responsible for most of the mechanisms of the CO<sub>2</sub> splitting. These electrons start moving to the electrodes, where they concentrate, under the effect of the electric field. During their movement, they can collide with other species present in the reactor, producing new reactions, such as ionization, dissociation, etc. The determination of the spatial distribution of electrons is essential to find the kinetic energy of the discharge.

The electron density inside the plasma reactor for times 2, 6, 10, 14, and 18 ms are shown in Figure 11. During this time, when a positive voltage was applied, the electrons were concentrated in the powered electrode. They moved inside the plasma reactor to the



surface electrode, where they were lost by recombination with its positive charge. When the voltage applied on the electrodes changed, these electrons moved to the ground electrode.

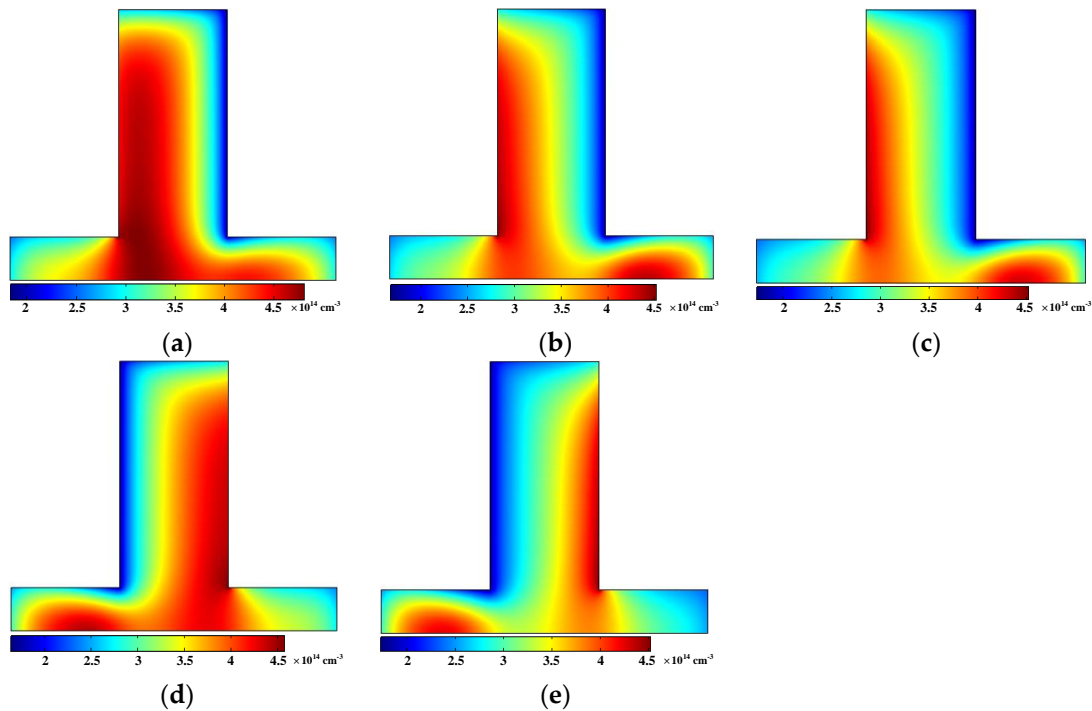


**Figure 11.** Spatial distribution of the electron density at time (a) 2 ms, (b) 6 ms, (c) 10 ms, (d) 14 ms, and (e) 18 ms for the reactor at 22 kV AC voltage and 1 cm distance between electrodes.

In the model results, high values of electron density inside the inlet/outlet pipes were observed, which means that these pipes contained high levels of chemical activity even though the electric field was low.

The experimental results were time-averaged values over the measuring period. Then, to compare with the experimental results, the time averages of the simulated electron density over a period ( $T = 20$  ms) were performed for the radial position  $r = 15$  mm, where the lens was focused. The results of these calculations are plotted in Figure 8b. A close agreement between the experimental results and this averaged result was found, which supports the soundness of the model.

### 3.2.3. Electron Temperature

In plasma dominated by electron interactions, its chemistry depends on the kinetic energy of these particles. The electrons take the energy from the electric field and share their energy with other particles by collisions. The electron temperature is a measure of the kinetic energy of the electrons.

Figure 12 plots the dependence of the electron temperature on the positions for times 2, 6, 10, 14, and 18 ms. The highest values of the electron temperature corresponded to positions where this field was highest, i.e., the powered electrode for positive voltage and the ground electrode for negative voltage. Otherwise, the electron temperature in the inlet/outlet pipes was lower by the low electric field in these zones.

The model results of electron temperature have also been averaged over the period ( $T = 20$  ms). The averaged values for  $r = 15$  mm are compared with the experimental measures of rotational, vibrational, and excitation temperatures in Figure 7b. The values of the theoretical electron temperatures were higher than these temperatures, which is typical of a 2-temperature plasma, characterized by the following relation between the temperatures:  $T_e \gtrsim T_{exc} > T_v > T_r \sim T_g$  [47].

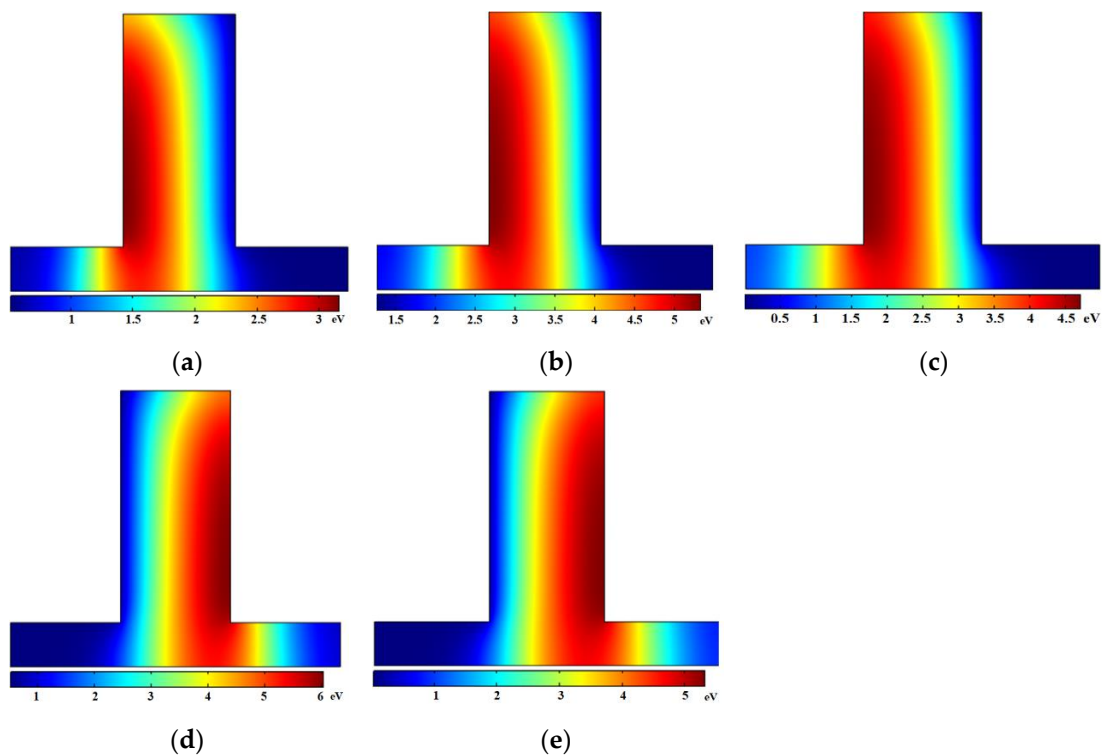


**Figure 12.** Spatial distribution of the electron temperature for times (a) 2 ms, (b) 6 ms, (c) 10 ms, (d) 14 ms, and (e) 18 ms for the reactor at 22 kV AC voltage and 1 cm distance between electrodes.

#### 3.2.4. CO<sub>2</sub> Splitting

The high values of electron density and temperature indicate that the chemistry in the AC-PPP reactor was dominated by the collisions of electrons with CO<sub>2</sub> ground state molecules. As predicted by the model, the most relevant mechanisms of CO<sub>2</sub> splitting were:

- the electron impact dissociation (or dissociative de-excitation collision) producing CO and O (see reactions 7 and 9 in Table 1),
- the electron ionization producing CO<sub>2</sub><sup>+</sup> ions (see reaction 12 in Table 1),
- the electron dissociative attachment producing CO molecules and O<sup>-</sup> ions (see reaction 15 in Table 1).

These mechanisms align with those proposed by Bogaerts et al. [48] for pure CO<sub>2</sub> splitting. The energy required by these three processes is higher than that needed for splitting by C=O bond breaking (CO<sub>2</sub> → CO + ½O<sub>2</sub>), i.e., 279.8 kJ/mol. This explains the low energy efficiency found for this plasma, i.e., lower than 6%.

The distribution of the four formed species: CO<sub>2</sub><sup>+</sup>, CO, O, O<sub>2</sub>, and O<sup>-</sup> were studied to identify the reactions that dominated in each part of the reactor.

#### Density of CO<sub>2</sub><sup>+</sup> Ion

Figure 13 shows the spatial distribution of the density of CO<sub>2</sub><sup>+</sup> ions formed for times, 2, 6, 10, 14, and 18 ms. In contrast with the electrons which moved toward the power electrode during the positive voltage applied (2, 6, and 10 ms) and were aggregated there, the electric field accelerated the produced positive ions CO<sub>2</sub><sup>+</sup> in the direction of this field. If a CO<sub>2</sub><sup>+</sup> ion obtains enough acceleration from the electric field, it collides with the background gas molecules and ionizes them. However, this phenomenon rarely happens in high electron density plasmas, where CO<sub>2</sub><sup>+</sup> ions are less effective than the electrons in the impacting ionization process. As shown in Figure 13, the CO<sub>2</sub><sup>+</sup> ions accumulated near the ground electrode during the positive voltage applied, and they accumulated in the powered electrode with the negative voltages.

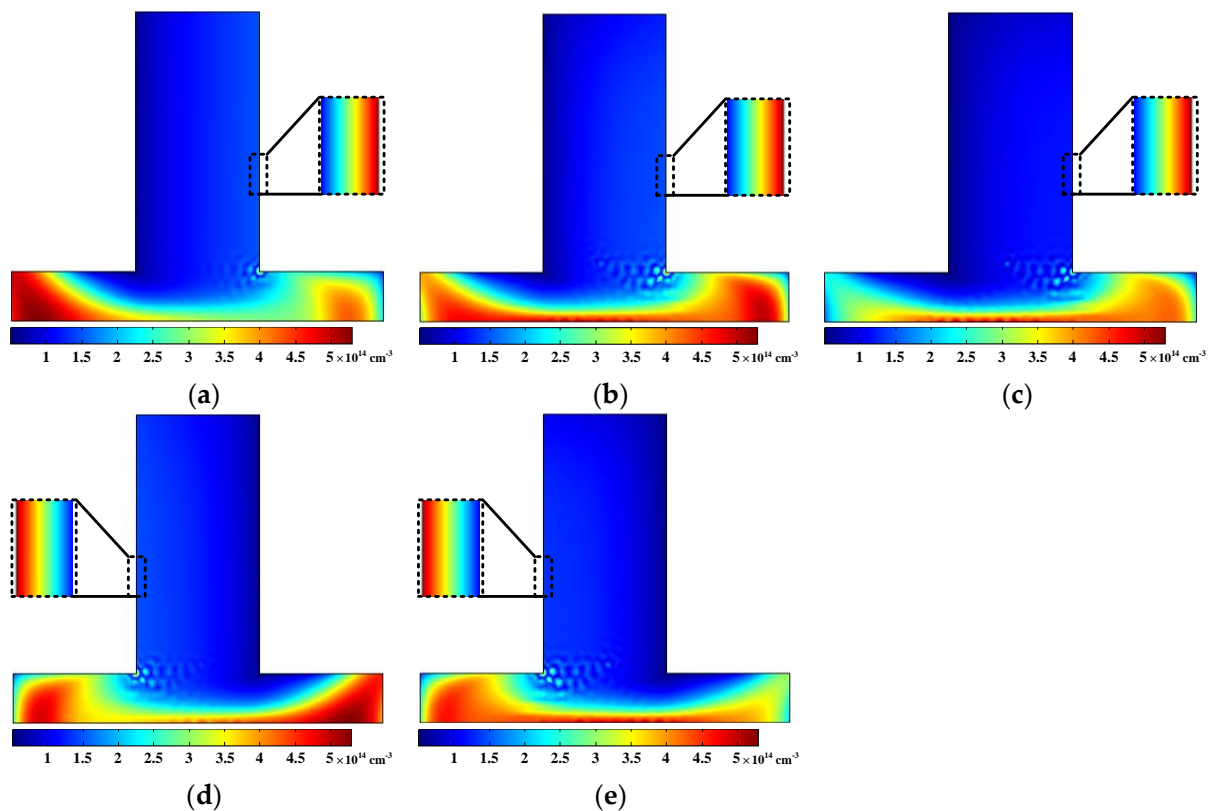


**Figure 13.** Spatial distribution of the  $\text{CO}_2^+$  density for times (a) 2 ms, (b) 6 ms, (c) 10 ms, (d) 14 ms, and (e) 18 ms for the reactor at 22 kV AC voltage and 1 cm distance between electrodes.

The maximum values of the  $\text{CO}_2^+$  density were found inside the metallic inlet/outlet pipes. The positive ions accumulated in this zone because they did not move toward the electrodes due to the low electric field inside the pipes. However, the  $\text{CO}_2^+$  ion is an unstable species and will be quickly recombined with electrons or negative ions  $\text{O}_2^-$  to convert to CO and O, and/or  $\text{O}_2$  [48].

#### Density of Neutral Species CO, O, and $\text{O}_2$

The densities of the neutral species CO and O generated inside the plasma discharge medium of the developed AC-PPP reactor at times 2, 6, 10, 14, and 18 ms are presented in Figures 14 and 15. These neutral species were produced near the powered electrode during the positive voltage and the ground electrode during the negative voltage. This was due to the high electron density near the electrodes, which produced the dissociation and attachment processes of the neutral species in these regions.

The maximum values of CO and O densities are equal to  $4.7 \times 10^{11} \text{ cm}^{-3}$  and  $2.3 \times 10^{11} \text{ cm}^{-3}$ , respectively. The maximum CO density is higher than O because this molecule is produced by two mechanisms, electron impact dissociation (reaction 7 and 9) and electron dissociative attachment (reaction 15). CO is a relatively stable molecule that can recombine with O and  $\text{O}^-$  to form new  $\text{CO}_2$  when the residence time is high [48]. However, the O atoms recombine quickly into oxygen molecules,  $\text{O}_2$  and/or ozone,  $\text{O}_3$ .

Oxygen molecules,  $\text{O}_2$ , are formed mainly by the reaction of oxygen atoms with the  $\text{CO}_2$  gas through neutral dissociation and 3-body recombination, reactions 17 and 20, respectively. Figure 16 shows the model results of the spatial distribution of the  $\text{O}_2$  density at times 2, 6, 10, 14, and 18 ms. The maximum values of this density correspond to positions where O and  $\text{CO}_2$  densities are higher.

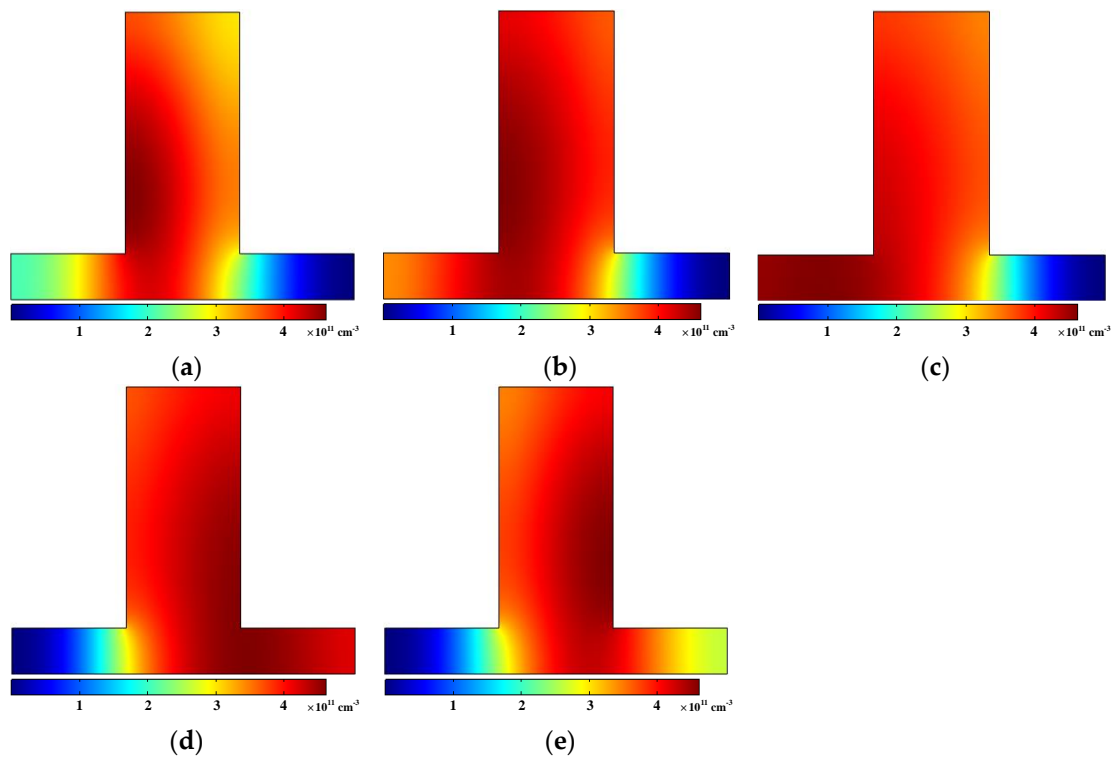


**Figure 14.** Spatial distribution of the CO density for times (a) 2 ms, (b) 6 ms, (c) 10 ms, (d) 14 ms, and (e) 18 ms for the reactor at 22 kV AC voltage and 1 cm distance between electrodes.

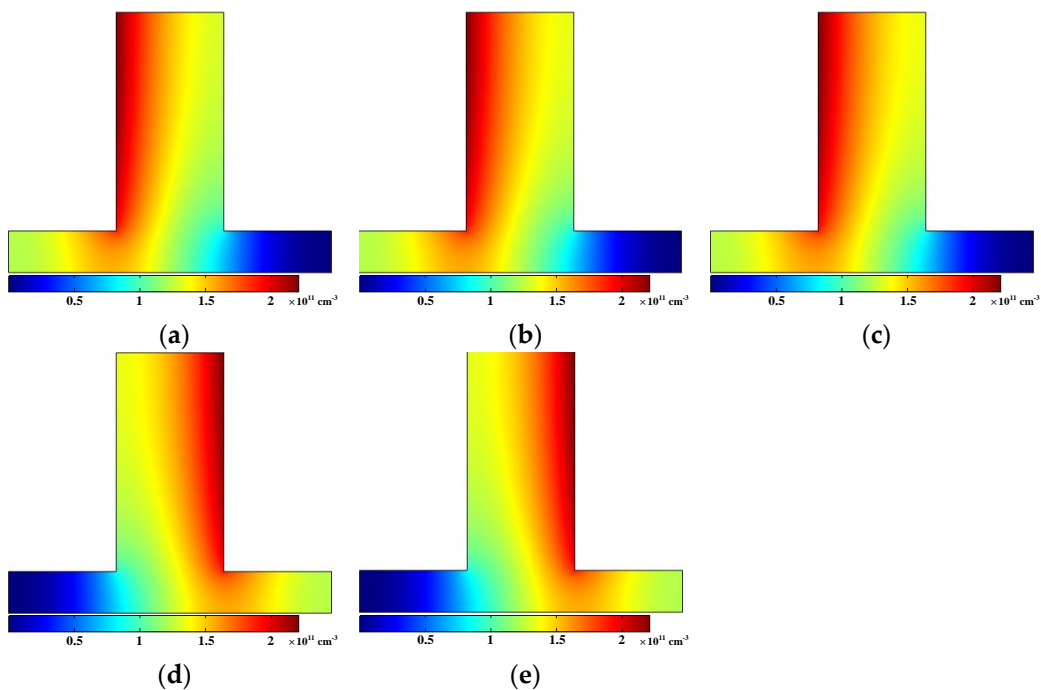


**Figure 15.** Spatial distribution of the O density for times (a) 2 ms, (b) 6 ms, (c) 10 ms, (d) 14 ms, and (e) 18 ms for the reactor at AC 22 kV voltage and 1 cm distance between electrodes.

Density of O<sup>-</sup> Ion

The electrons traveling to the electrodes can produce negative ions by attachment with the species present in the plasma. This was the case for the negative ion O<sup>-</sup> (reaction 15).

The spatial distribution of the density of  $O^-$  ions produced by this process for times 2, 6, 10, 14, and 18 ms are shown in Figure 17.

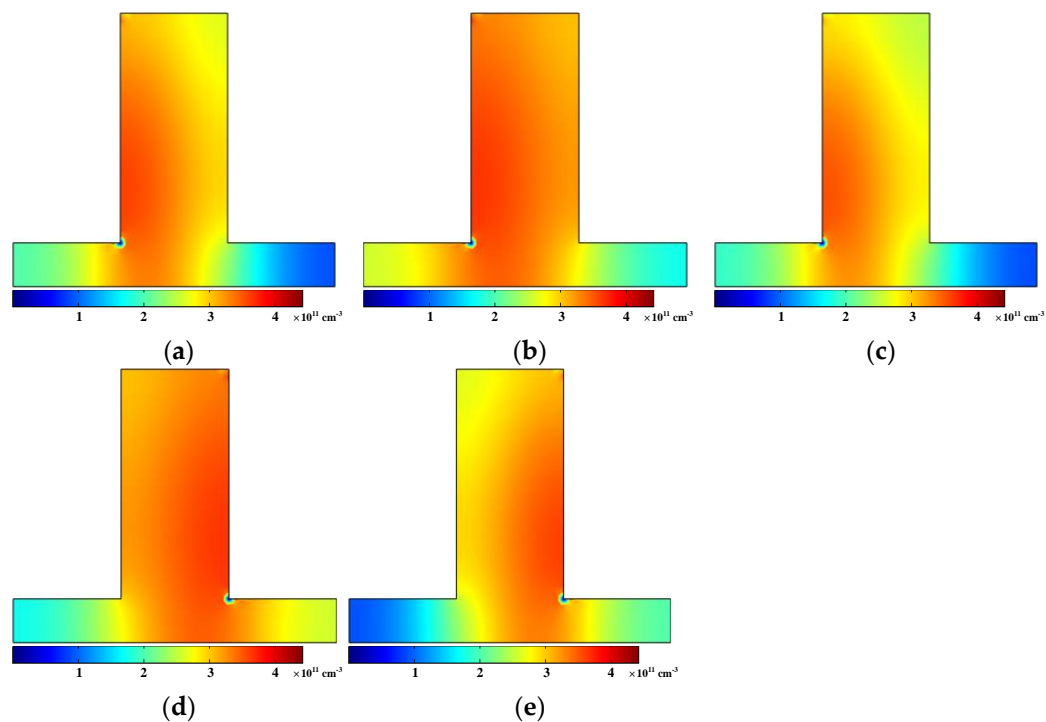


**Figure 16.** Spatial distribution of the  $O_2$  density for times (a) 2 ms, (b) 6 ms, (c) 10 ms, (d) 14 ms, and (e) 18 ms for the reactor at AC 22 kV voltage and 1 cm distance between electrodes.

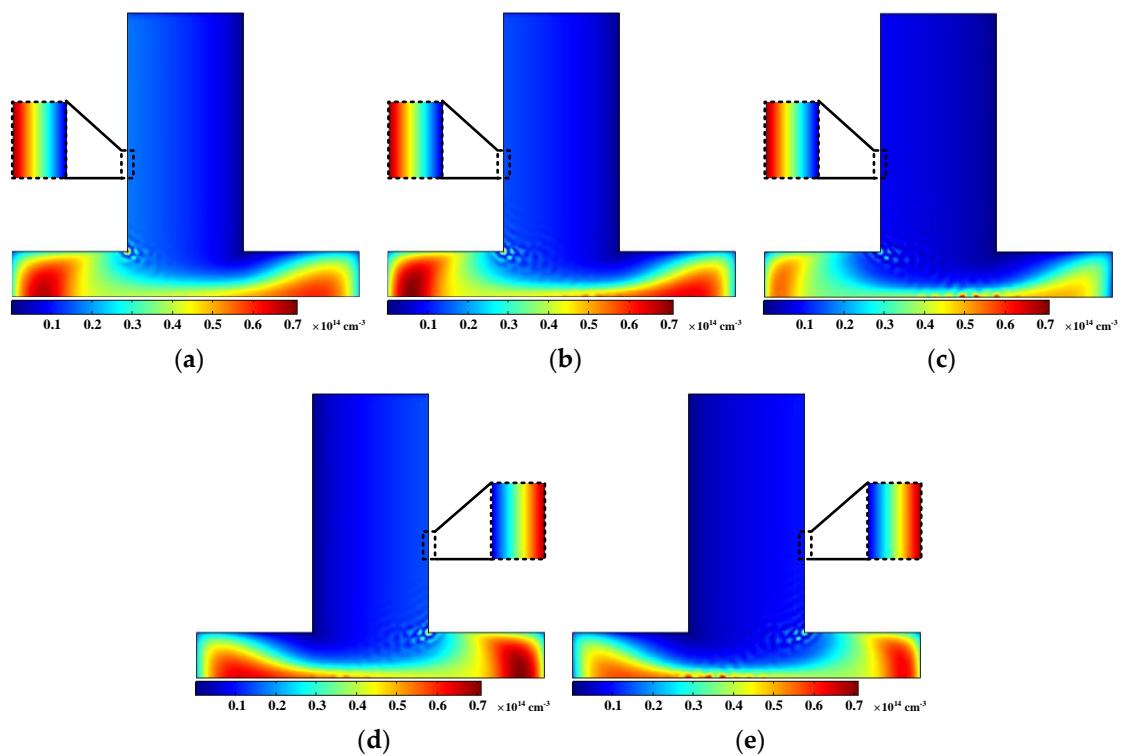


**Figure 17.** Spatial distribution of the  $O^-$  ion density for times (a) 2 ms, (b) 6 ms, (c) 10 ms, (d) 14 ms, and (e) 18 ms for the reactor at 22 kV AC voltage and 1 cm distance between electrodes.

The negative  $O^-$  ions moved toward the electrodes and were aggregated there according to electron density. This negative oxygen ion density increased quickly and became constant after the first millisecond.

The electron dissociative attachment that produced the  $O^-$  ions was higher in the inlet/outlet pipes. The high densities and low temperatures in these positions favored the electron attachment in these zones.

#### Density of $CO_2$ Molecules

Reactions 7, 9, and 15 mainly describe the  $CO_2$  conversion and the density distribution of this molecule in the reactor. The spatial distribution of  $CO_2$  density between the two electrodes inside the AC-PPP reactor is presented in Figure 17. The  $CO_2$  density decreased near the electrodes due to the high values of electron density and temperature in this position. A zoom of the zone near the electrodes was plotted in Figure 18. Due to the plasma is still active inside the conductor inlet/outlet pipes, the  $CO_2$  was also decomposed inside these pipes.

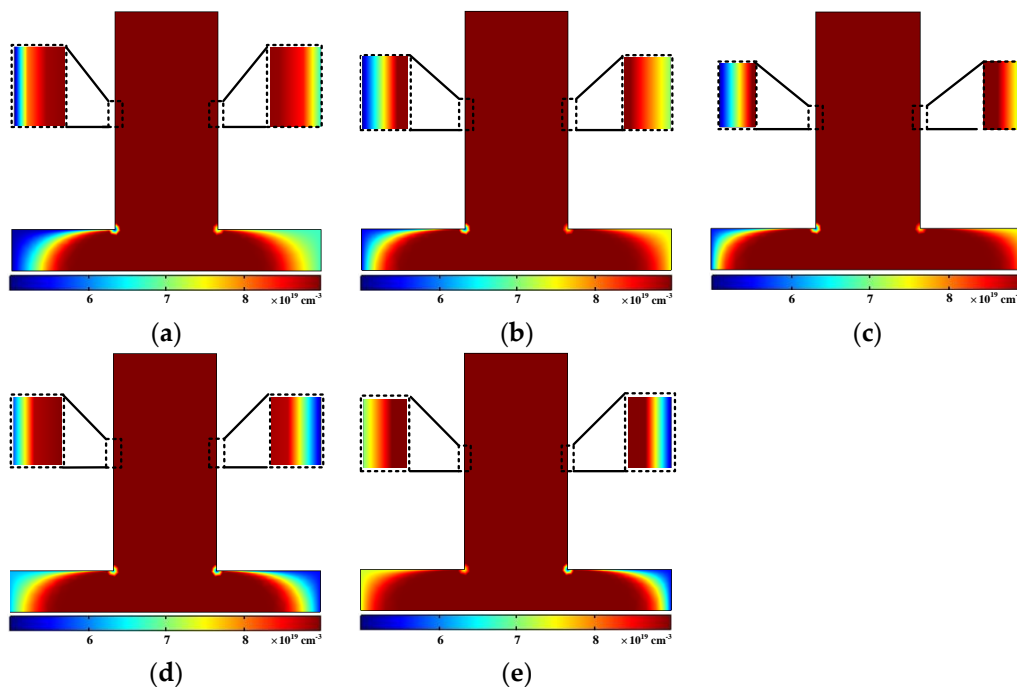


**Figure 18.** Spatial distribution of  $CO_2$  density at time (a) 2 ms, (b) 6 ms, (c) 10 ms, (d) 14 ms, and (e) 18 ms for the reactor at AC 22 kV voltage and 1 cm distance between electrodes.

As is shown, during the positive voltage (2, 6, and 10 ms), the maximum  $CO_2$  decomposition was near the powered electrode, where the electron density was highest. Conversely, the maximum value was near the ground electrode during the negative voltage (14 and 18 ms). A theoretical estimation of the  $CO_2$  conversion factor was made with the time averages of the  $CO_2$  density over a period,  $T = 20$  ms, in the outlet tube position, which could be compared with the experimental results of gas chromatography. A good agreement between experimental and theoretical results was found (see Figure 4a).

#### 4. Conclusions

In this study, a new AC-PPP reactor for  $CO_2$  remediation was presented. We undertook experimental measurements by gas chromatography and optical emission spectroscopy to characterize and determine its capacity for  $CO_2$  decomposition. The  $CO_2$  conversion and energy efficiency were obtained by the GC method and compared with other plasma sources. It was found that  $CO_2$  conversion in the developed plasma reactor was close to

25%, higher than GA, and similar to DBD. Although the energy efficiency of the AC-PPP reactor (near 6.1%) is lower than the maximum values of the other technologies, this AC-PPP reactor could be very useful and suitable for industrial applications due to its simple design and capacity to work with AC at atmospheric pressure.

The experimental electron density and the rotational, vibrational, and excitation temperatures were calculated by OES spectroscopy. The high values of vibration and excitation temperatures, around 5100 K and 18,300 K, respectively, compared with the rotational temperature (~2000 K), show that it is a 2-temperature plasma, where the electrons have higher kinetic energy and are mainly responsible for the splitting reactions. This result was confirmed by the high electron number density found experimentally in this discharge with a maximum value of  $5 \times 10^{14} \text{ cm}^{-3}$ .

A 2-D fluid model was developed to simulate the kinetics of CO<sub>2</sub> decomposition in this plasma. The temporal and spatial behaviors of the densities of CO<sub>2</sub> and the formed species inside the plasma reactor were calculated according to this model. According to the theoretical results, the charged species oscillated between the electrodes at each cycle of the AC potential with a frequency of 50 Hz. This movement can cause more ionization in the plasma reactor and a better CO<sub>2</sub> decomposition by increasing collisions.

The model has demonstrated that the main mechanisms of CO<sub>2</sub> splitting were the electron impact dissociation, the electron ionization, and the electron dissociative attachment. The species O<sup>-</sup> and CO<sub>2</sub><sup>+</sup> ions, CO and O<sub>2</sub> molecules, and O atoms were formed by these mechanisms. The spatial distributions of these species were calculated. The results of the model showed that the discharge was also formed inside the inlet and outlet pipes. This extension of the discharge influences the improvement of CO<sub>2</sub> conversion by this reactor.

The distribution of the CO<sub>2</sub> density was also determined. A final reduction of this molecule of about 22% could be achieved after the passing of gas along the reactor. This CO<sub>2</sub> conversion agreed with experimental values of this parameter obtained by GC.

The electron density and temperature averaged over a period was calculated. The value and behavior of this electron density under study conditions also agreed with the experimental results.

We consider that the developed 2-D model has been shown to be valid for describing and understanding the main processes that occur in the reactor and which lead to the decomposition of CO<sub>2</sub> and its transformation into other species. This type of reactor could contribute to the optimization of working conditions and improvements in reactor design.

**Author Contributions:** A.B. designed the research; A.B., S.I.M., A.F. and S.K. performed the experiments and the numerical calculations; A.B. and A.R. supervised the research (experiments and calculations); A.B., A.R. and D.A.K. were involved in writing and editing the manuscript; A.R. and D.A.K. were involved in funding acquisition. All authors have read and agreed to the published version of the manuscript.

**Funding:** The research and APC was funded by the project BUT InterAcademic Partnerships (PPI/APM/2018/1/00033/U/001) of The Polish National Agency for Academic Exchange.

**Institutional Review Board Statement:** Not applicable.

**Informed Consent Statement:** Not applicable.

**Data Availability Statement:** The data that support the findings of this study are available from the corresponding author upon reasonable request.

**Acknowledgments:** The authors are grateful for the part-financing of the study by the Andalusian Regional Government (Research Groups FQM-136). This publication was financed within the project BUT InterAcademic Partnerships (PPI/APM/2018/1/00033/U/001) of The Polish National Agency for Academic Exchange. The study was conducted in the Scientific Cooperation Agreement, "The possibility of the renewable energy sources usage in the context of improving energy efficiency and air quality in the buildings and civil constructions" between BUT and UCO supported by science research funds from the Bialystok University of Technology WZ/WB-IIS/9/2019.

**Conflicts of Interest:** The authors declare no conflict of interest.

## References

1. Lieberman, M.A.; Lichtenberg, A.J. *Principles of Plasma Discharges and Materials Processing*, 2nd ed.; John Wiley & Sons: New York, NY, USA, 2005; pp. 122–250.
2. Kogelschatz, U. Dielectric-barrier discharges: Their history, discharge physics, and industrial applications. *Plasma Chem. Plasma Process.* **2003**, *23*, 1–46. [[CrossRef](#)]
3. Aresta, M. *Carbon Dioxide as Chemical Feedstock*, 1st ed.; John Wiley & Sons: New York, NY, USA, 2010; pp. 152–180.
4. Kraus, M.; Eliasson, B.; Kogelschatz, U.; Wokaun, A. CO<sub>2</sub> reforming of methane by the combination of dielectric-barrier discharges and catalysis. *Phys. Chem. Chem. Phys.* **2001**, *3*, 294–300. [[CrossRef](#)]
5. Fridman, A. *Plasma Chemistry*, 1st ed.; Cambridge University Press: Cambridge, UK, 2008; pp. 231–254.
6. Trencheva, G.; Nikiforov, A.; Wanga, W.; Kolevc, S.; Bogaerts, A. Atmospheric pressure glow discharge for CO<sub>2</sub> conversion: Model-based exploration of the optimum reactor configuration. *Chem. Eng. J.* **2019**, *362*, 830–841. [[CrossRef](#)]
7. Snoeckx, R.; Bogaerts, A. Plasma technology—A novel solution for CO<sub>2</sub> conversion? *Chem. Soc. Rev.* **2017**, *46*, 5805–5863. [[CrossRef](#)] [[PubMed](#)]
8. Li, D.; Li, X.; Bai, M.; Tao, X.; Shang, S.; Dai, X.; Yin, Y. CO<sub>2</sub> Reforming of CH<sub>4</sub> by Atmospheric Pressure Glow Discharge Plasma: A High Conversion Ability. *Int. J. Hydrogen Energy* **2009**, *34*, 308–313. [[CrossRef](#)]
9. Li, H.; Zhou, Y.; Donnelly, V.M. Optical and Mass Spectrometric Measurements of the CH<sub>4</sub>–CO<sub>2</sub> Dry Reforming Process in a Low Pressure, Very High Density, and Purely Inductive Plasma. *J. Phys. Chem. A* **2020**, *124*, 7271–7282. [[CrossRef](#)] [[PubMed](#)]
10. Li, M.; Xu, G.; Tian, Y.; Chen, L.; Fu, H. Carbon Dioxide Reforming of Methane Using DC Corona Discharge Plasma Reaction. *J. Phys. Chem. A* **2004**, *108*, 1687–1693. [[CrossRef](#)]
11. Yu, Q.; Kong, M.; Liu, T.; Fei, J.; Zheng, X. Characteristics of the decomposition of CO<sub>2</sub> in a dielectric packed-bed plasma reactor. *Plasma Chem. Plasma Process.* **2012**, *32*, 153–163. [[CrossRef](#)]
12. Wang, Q.; Shi, H.; Yan, B.; Jin, Y.; Cheng, Y. Steam enhanced carbon dioxide reforming of methane in DBD plasma reactor. *Int. J. Hydrogen Energy* **2011**, *36*, 8301–8306. [[CrossRef](#)]
13. Liu, C.J.; Xu, G.H.; Wang, T. Non-thermal plasma approaches in CO<sub>2</sub> utilization. *Fuel Process. Technol.* **1999**, *58*, 119–134. [[CrossRef](#)]
14. Shrestha, R.; Tyata, R.; Subedi, D. Estimation of electron temperature in atmospheric pressure dielectric barrier discharge using line intensity ratio method. *Kathmandu Univ. J. Sci. Eng. Technol.* **2013**, *8*, 37–42. [[CrossRef](#)]
15. Raju, G.G. *Gaseous Electronics Theory and Practice*, 1st ed.; CRC Press Taylor & Francis Group: New York, NY, USA, 2006; pp. 351–423.
16. Torres, J.; Van De Sande, M.J.; Van Der Mullen, J.; Gamero, A.; Sola, A. Stark broadening for simultaneous diagnostics of the electron density and temperature in atmospheric microwave discharges. *Spectrochim. Acta B At. Spectrosc.* **2006**, *61*, 58–68. [[CrossRef](#)]
17. Laux, C.O.; Spence, T.G.; Kruger, C.H.; Zare, R.N. Optical diagnostics of atmospheric pressure air plasmas. *Plasma Sources Sci. Technol.* **2003**, *12*, 125. [[CrossRef](#)]
18. Dorai, R. Modeling of Plasma Remediation of NO<sub>x</sub> Using Global Kinetic Models Accounting for Hydrocarbons. Master's Thesis, University of Illinois at Urbana-Champaign, Champaign, IL, USA, 2000.
19. Hayashi Database. Available online: [www.lxcat.net/Hayashi](http://www.lxcat.net/Hayashi) (accessed on 19 March 2020).
20. Wang, W.; Berthelot, A.; Kolev, S.; Tu, X.; Bogaerts, A. CO<sub>2</sub> conversion in a gliding arc plasma: 1D cylindrical discharge model. *Plasma Sources Sci. Technol.* **2016**, *25*, 065008. [[CrossRef](#)]
21. PLASIMO Software. Plasma Matters. Eindhoven University of Technology. Available online: <http://plasimo.phys.tue.nl/> (accessed on 19 March 2020).
22. Moravej, M.; Yang, X.; Hicks, R.F.; Penelon, J.; Babayan, S.E. A radio-frequency nonequilibrium atmospheric pressure plasma operating with argon and oxygen. *J. Appl. Phys.* **2006**, *99*, 093305. [[CrossRef](#)]
23. Kozák, T.; Bogaerts, A. Splitting of CO<sub>2</sub> by vibrational excitation in non-equilibrium plasmas: A reaction kinetics model. *Plasma Sources Sci. Technol.* **2014**, *23*, 045004. [[CrossRef](#)]
24. Mikoviny, T.; Kocan, M.; Matejcik, S.; Mason, N.J.; Skalny, J.D. Experimental study of negative corona discharge in pure carbon dioxide and its mixtures with oxygen. *J. Phys. Appl. Phys.* **2004**, *37*, 64–73. [[CrossRef](#)]
25. Barkhordari, A.; Mirzaei, S.I.; Falahat, A.; Rodero, A. Numerical and experimental study of an Ar/CO<sub>2</sub> plasma in a point-to-plane reactor at atmospheric pressure. *Spectrochim. Acta Part B At. Spectrosc.* **2021**, *177*, 106048.
26. Chiper, A.S.; Chen, W.; Mejlholm, O.; Dalgaard, P.; Stamate, E. Atmospheric pressure plasma produced inside a closed package by a dielectric barrier discharge in Ar/CO<sub>2</sub> for bacterial inactivation of biological samples. *Plasma Sources Sci. Technol.* **2011**, *20*, 025008. [[CrossRef](#)]
27. Prigogine, I. Chemical kinetics and dynamics. *Ann. N. Y. Acad. Sci.* **2003**, *988*, 128–132. [[CrossRef](#)] [[PubMed](#)]
28. Marrero, T.; Mason, E.A. Gaseous diffusion coefficients. *J. Phys. Chem. Ref. Data* **1972**, *1*, 3–118. [[CrossRef](#)]
29. Jasper, A.W.; Miller, J.A. Lennard–Jones parameters for combustion and chemical kinetics modeling from full-dimensional intermolecular potentials. *Combust. Flame* **2014**, *161*, 101–110. [[CrossRef](#)]
30. Raizer, Y.P.; Kisin, V.I.; Allen, J.E. *Gas Discharge Physics*, 1st ed.; Springer: Berlin/Heidelberg, Germany, 1991; pp. 283–301.
31. Becker, M.; Loffhagen, D.; Schmidt, W. A stabilized finite element method for modeling of gas discharges. *Comput. Phys. Commun.* **2009**, *180*, 1230–1241. [[CrossRef](#)]



32. Hagelaar, G.; De Hoog, F.; Kroesen, G. Boundary conditions in fluid models of gas discharges. *Phys. Rev. E* **2000**, *62*, 1452. [[CrossRef](#)] [[PubMed](#)]
33. Aerts, R.; Somers, W.; Bogaerts, A. Carbon dioxide splitting in a dielectric barrier discharge plasma: A combined experimental and computational study. *ChemSusChem* **2015**, *8*, 702–716. [[CrossRef](#)] [[PubMed](#)]
34. Reyes, P.G.; Gomez, A.; Vergara, J.; Martinez, H.; Torres, C. Plasma diagnostics of glow discharges in mixtures of CO<sub>2</sub> with noble gases. *Rev. Mex. Fis.* **2017**, *63*, 363–371.
35. Shimizu, K.; Oda, T. Emission spectrometry for discharge plasma diagnosis. *Sci. Technol. Adv. Mater.* **2001**, *2*, 577. [[CrossRef](#)]
36. Maouhoub, E. Determination of the real experimental composition of the Ar-CO<sub>2</sub> mixture from calculation of the atomic excitation temperature. *EPJ Appl. Phys.* **1998**, *3*, 81–89. [[CrossRef](#)]
37. Griem, H.R. *Plasma Spectroscopy*, 2nd ed.; Cambridge University Press: Cambridge, UK, 2005; pp. 342–390.
38. Gigosos, M.A.; Cardenoso, V. New plasma diagnosis tables of hydrogen Stark broadening including ion dynamics. *J. Physical B-At. Mol. Opt.* **1996**, *29*, 4795. [[CrossRef](#)]
39. Belostotskiy, S.G.; Ouk, T.; Donnelly, V.M.; Economou, D.J.; Sadeghi, N. Gas temperature and electron density profiles in an argon dc microdischarge measured by optical emission spectroscopy. *J. Phys. D Appl. Phys.* **2010**, *107*, 053305. [[CrossRef](#)]
40. Nikiforov, A.Y.; Leys, C.; Gonzalez, M.A.; Walsh, J.L. Electron density measurement in atmospheric pressure plasma jets: Stark broadening of hydrogenated and non-hydrogenated lines. *Plasma Sources Sci. Technol.* **2015**, *24*, 034001. [[CrossRef](#)]
41. Boffard, J.B.; Lin, C.C.; DeJoseph, C.A., Jr. Application of excitation cross sections to optical plasma diagnostics. *J. Phys. D Appl. Phys.* **2004**, *37*, R143. [[CrossRef](#)]
42. Mehr, F.J.; Biondi, M.A. Electron-temperature dependence of electron-ion recombination in Argon. *Phys. Rev.* **1968**, *176*, 322. [[CrossRef](#)]
43. Pandhija, S.; Rai, A.K. In situ multielemental monitoring in coral skeleton by CF-LIBS. *Appl. Physical B* **2009**, *94*, 545–552. [[CrossRef](#)]
44. Braun, D.; Gibalov, V.; Pietsch, G. Two-dimensional modelling of the dielectric barrier discharge in air. *Plasma Sources Sci. Technol.* **1992**, *1*, 166. [[CrossRef](#)]
45. Moreno Wandurraga, S.H. Reduced Reaction Kinetics Model for CO<sub>2</sub> Dissociation in Non-Thermal Microwave Discharges. Master's Thesis, Delft University of Technology, Delft, The Netherlands, 2015.
46. Khodja, K.; Belasri, A. Sheath formation study in Ne-Xe DBD discharge. *Radiat. Eff. Defects Solids* **2012**, *167*, 734–742. [[CrossRef](#)]
47. Staack, D.; Farouk, B.; Gutsol, A.; Fridman, A. Characterization of a dc atmospheric pressure normal glow discharge. *Plasma Sources Sci. Technol.* **2005**, *14*, 700. [[CrossRef](#)]
48. Bogaerts, A.; Snoeckx, R.; Trenchev, G.; Wang, W. *Plasma Chemistry and Gas Conversion*; BoD-Books on Demand: Norderstedt, Germany, 2018.